Macromolecules

pubs.acs.org/Macromolecules Article

Utilization of Block Copolymers to Understand Water Vaporization Enthalpy Reduction in Uniform Pores

Joel M. Serrano, Tianyu Liu, Dong Guo, Zacary L. Croft, Ke Cao, Assad U. Khan, Zhen Xu, Elsaid Nouh, Shengfeng Cheng, and Guoliang Liu*

Cite This: *Macromolecules* 2022, 55, 4803–4811 Read Online

ACCESS | Metrics & More | Article Recommendations | Supporting Information

ABSTRACT: Solar desalination, a technique converting solar irradiation to heat for evaporating saltwater and generating freshwater, has garnered much attention because of the ever-growing global demand for potable water. Herein, we utilize block copolymer-based porous carbon fibers with well-controlled porous structures to investigate the latent heat reduction in mesopores and micropores. The porous carbon fibers achieve high energy efficiencies and solar desalination rates up to 3.8 kg m^{-2} h^{-1} under 1 sun irradiation owing to the >99% light absorption across the solar spectrum and reduced vaporization enthalpy of pore-confined water. The nanoconfinement effect of pores is evaluated by measuring evaporation enthalpies and rates for morphologically tailored carbon fibers with pore sizes ranging from ∼1 to ∼22 nm. Our results show a continuous reduction in an enthalpic energy of up to 43% as mesopore size decreases to ∼10.7 nm and then less reduction of only 14% with a further decrease in micropore size to <1 nm. The mesopores exhibit significantly enhanced evaporation rates compared with micropores due to the nanoscale confinement-related enthalpy reduction and water transport. This study provides insight into nanoconfinement effects with well-controlled pore sizes and contributes to further understanding and design of porous materials for future environmental applications.

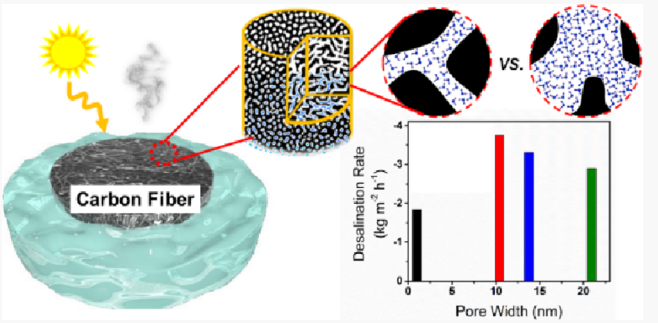

INTRODUCTION

A major challenge for the growing global population is the disparity between freshwater demand and supply. Although brackish and sea water are abundant, the energy required for desalination using current methods prevents wide access to potable desalinated water. Many technologies are under development to combat this problem by enhancing desalination efficiency.[1−3] Distillation and similar thermal-based methods produce water through vaporization and recondensation, yet they suffer from limited energy efficiencies.[4] Other systems, such as membrane-based reverse osmosis,[5] consume comparatively less energy than the thermal-based methods[6−8] but experience other issues such as membrane biofouling, high working pressures, and intensive maintenance, in addition to large footprints and costly infrastructures.[9,10] Alternatively, solar desalination requires much lower energy input and less complex infrastructures.[11−13] Solar also provides off-grid and low-to-no waste production of potable water from high-salinity sources.[14,15] Thus, solar desalination has gained increasing popularity in confronting the aforementioned challenges faced by traditional systems, especially in regions with limited access to large-scale infrastructures.[16,17]

Solar energy provides a sustainable source for water vapor generation, but an effective solar desalination system demands both high light absorption and photothermal conversion efficiencies.[18,19] The literature has focused on strategies ranging from initial energy harvesting to final recondensation.[20−22] For example, ultra-absorbers such as plasmonic nanoparticles highlighted the importance of solar-to-thermal energy conversion efficiency.[23−25] Strategized materials, such as thermal-concentration ceramics[26] and nanostructured gels,[27] addressed the issue of parasitic heat loss by localizing heat and reducing energy dissipation. Heat recovery was realized by coupling photonics with distillation to further mitigate energy loss.[28] These strategies highlight the rationales of increasing solar energy uptake and decreasing energy loss, all of which enhance solar desalination efficiency. However, another fundamental and yet important mechanism remains largely underdeveloped in the minimization of the inherent energy requirement for the phase change of water from liquid to vapor.[18,29]

Owing to the large vaporization enthalpy of water, even an ultra-high efficient system—without any latent heat reduc-

Received: January 17, 2022
Revised: May 5, 2022
Published: May 23, 2022

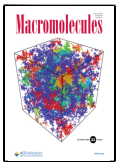

https://doi.org/10.1021/acs.macromol.2c00092
Macromolecules 2022, 55, 4803−4811

tion—could only achieve a theoretical maximum evaporation rate of 1.6 kg m^{-2} h^{-1} under 1 sun irradiation.[4] New technologies are under development to address this challenge by lowering the energy required for vaporization.[30−33] Previous experimental and simulation studies also point toward the potential for achieving high desalination efficiency using a nanoconfinement approach, which reduces the intermolecular interactions between adjacent water molecules and thus water density.[34−37] Despite numerous reports using porous materials such as carbon foam[38] and pyrolyzed biomasses,[39−41] for solar-thermal desalination, the differing effects of mesopores and micropores on nanoconfinement of water remain unclear.[42−44] To this end, we designed a system with controllable pore sizes, utilizing our recently developed block copolymer-based porous carbon fibers (PCFs), to elucidate the relationship between nanoconfinement and water vaporization enthalpy.

Our judiciously selected block copolymer precursor, poly(methyl methacrylate)-*block*-poly(acrylonitrile) (PMMA-*b*-PAN), provides a controlled, template-free method for producing PCFs *via* sequential electrospinning, oxidation, and pyrolysis (Figure 1). Owing to the unique capability of

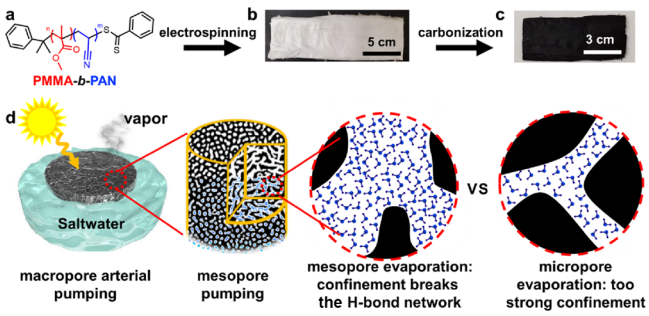

Figure 1. Scheme of block copolymer-based porous carbon fibers for solar desalination. (a) PMMA-*b*-PAN block copolymers were synthesized and electrospun to (b) polymer fiber mats and then converted to (c) porous carbon fibers *via* carbonization. (d) The fibers were semi-submerged in saltwater. Water traveled through the inter-fiber macropores via arterial pumping and then toward the interiors of the fibers *via* mesopore pumping. The interior mesopores and micropores pose different nanoconfinement effects on water.

microphase separation, the block copolymer forms well-defined mesoscale structures for formation into mesopores. The size of the mesopores is highly uniform, as governed by the block copolymer molecular weight and composition. In addition, the intrinsically semi-crystalline PAN develops well-controlled micropores during the carbonization process. Therefore, PMMA-*b*-PAN provides an exceptional platform for investigating the effects of mesopores and micropores on solar water vaporization. PCFs are expected to exhibit excellent solar desalination efficiency because (i) PCFs absorb >99% of light in the solar spectrum and have a high solar energy harvesting capability; (ii) electrospinning creates inter-fiber macropores for rapid water transport from the bulk to the inter-fiber space and the interconnected meso- and micropores; (iii) the nanoconfinement accelerates water evaporation by decreasing vaporization enthalpy;[45−47] and (iv) PCFs have enhanced heat transfer contained by thermal diffusion within the fiber mat. Consequently, the well-defined and tunable pore structures allow for an unprecedented opportunity to experimentally examine the evaporation behavior of water under varying nanoconfinement conditions.

With well-tuned pore sizes from ∼0.6 to 21.6 nm, our measurements showed that, for block copolymer-derived PCFs, the vaporization enthalpy diminished to ∼43% of the value for bulk water with decreasing mesopore sizes. The water evaporation rate reached a maximum of 3.8 kg m^{-2} h^{-1} under 1 sun irradiation, ∼9.5 times higher than the evaporation rate of bulk water. In contrast, PAN homopolymer-derived carbon fibers (CFs), with micropores of <2 nm and no mesopores, only reduced the latent heat for water vaporization by ∼14% and were significantly inferior for solar desalination. The nanoconfinement provided by the PCFs enables facile desalination and deepens the understanding of latent heat reduction induced by confinement (Figure 1). This work serves as a useful guide for material design in future environmental applications.

MATERIALS AND METHODS

Chemicals. Methyl methacrylate (MMA, ≥99%), acrylonitrile (AN, ≥99%), 2,2′-azobis(2-methylpropionitrile) (AIBN ≥98%), benzene (≥99%), aluminum oxide (activated, neutral, Brockmann Activity I), *N*,*N*-dimethylformamide (DMF, ≥99.7%), and dimethyl sulfoxide (DMSO, ≥99.9%) were purchased from Sigma-Aldrich. Cumyl dithiobenzoate (CDB) was synthesized *via* a previously reported pathway. Pumped methanol was used for polymer precipitation. MMA and AN were purified by alumina column filtration to remove inhibitors.[48]

Synthesis and Fabrication of Carbon Fibers. Poly(methyl methacrylate)-*block*-poly(acrylonitrile) (PMMA-*b*-PAN) was synthesized *via* reversible addition-fragmentation chain transfer (RAFT) polymerization according to a previous report with modifications.[49] First, a mixture of MMA (70.0 mL, 618 mmol), CDB (168.6 mg, 0.318 mmol), and AIBN (50.8 mg, 0.310 mmol) was dissolved in benzene (110 mL) in a 500 mL Schlenk flask. The solution was subjected to three cycles of freeze-pump-thaw (FPT) followed by back-filling with N_2 to remove dissolved oxygen gas. The reaction proceeded at 60 °C resulting in a PMMA macro-chain transfer agent (CTA). Three macro-CTAs were synthesized by polymerization at 60 °C for 14, 22, and 52 h, resulting in PMMA-C (41 kDa), PMMA-B (59 kDa), and PMMA-A (108 kDa), respectively (Figure S1). The PMMA macro-CTAs were precipitated in methanol, filtered, and dried under vacuum for 12 h.

The purified PMMA macro-CTAs were then used to synthesize PMMA-*b*-PAN block copolymers (BCP). The macro-CTAs were subject to the same molar ratios. The synthesis of BCP-B will serve as an example. BCP-B was synthesized by the mixture of PMMA-B macro-CTA (6.50 g, 110.1 μmol), AN (26.0 mL, 433.1 mmol), AIBN (4.4 mg, 27.0 μmol), and DMSO (72.2 mL). Note that, for both BCP-A and BCP-C, the molar ratios are exactly the same. The AIBN was added last to the mixture immediately preceding the three FPT cycles. The mixture was then heated in an oil bath at 65 °C under a N_2 atmosphere for 8 h, which resulted in precursors with PAN number-average molecular weights: BCP-B (36 kDa). Note that the same molar ratios were used for PMMA-A and PMMA-C; however, the reactions proceeded for 10 h (PMMA-A) and 12 h (PMMA-C), resulting in PAN molecular weights BCP-A (44 kDa) and BCP-C (66 kDa). The PMMA-*b*-PAN block copolymers were purified following the same steps as the PMMA macro-CTAs. The PAN homopolymer was synthesized with radical polymerization in a 250 mL Schlenk flask by adding AN (34.6 mL, 528 mmol), AIBN (15.08 mg, 91.83 mmol), *S*,*S*-dibenzyl trithiocarbonate (SSDT, 96.8 mg, 0.334 mmol), and DMSO (80 mL) into the mixture. The solution was subjected to three cycles of FPT and filled with N_2. The mixture was then heated at 60 °C for 12 h. The mixture was then diluted with 80 mL of DMF and then precipitated into MeOH. The precipitates were collected by filtration, washed with MeOH, and then dried in vacuo at 80 °C to remove the residual solvents.

The number-average molecular weights were measured with size exclusion chromatography (SEC) (EcoSEC HLC-8320GPC) equip-

https://doi.org/10.1021/acs.macromol.2c00092
Macromolecules 2022, 55, 4803−4811

ped with a light scattering detector (DynaPro Nanostar photometer) (Table 1). The block copolymers were then dissolved in DMF (18 wt %) overnight. The dissolved BCPs were electrospun at a flow rate of 0.020 mL min^{-1} with 18 kV (using high power supply, Model P030HP1, Acopian Technical Company) and collected onto an aluminum drum with a spin rate of ∼120 rpm. The as-spun fibers were oxidized at 280 °C with a heating rate of 1 °C min^{-1} for 8 h under air to stabilize the fibers and then pyrolyzed at 800 °C for 1 h at a heating rate of 10 °C min^{-1} in a tube furnace (Model STF55433C-1, Lindberg/Blue M) under a N_2 atmosphere (N_2 flow rate, 200 standard cubic centimeters per minute).

Table 1. Characteristics of Carbon Fibers PCF-A, PCF-B, PCF-C, and CF and the Precursor Polymers

fibers	polymer precursor	pore width (nm)	surface area (m^2 g^{-1})[a]	pore volume (cm^3 g^{-1})[b]
CF	PAN	<2	120	3.6
PCF-A	BCP-A	21.6	445	8.5
PCF-B	BCP-B	14.7	690	10.1
PCF-C	BCP-C	10.7	760	11.0

[a]Values based on N_2 physisorption. [b]Total pore volume of N_2 and CO_2 physisorption.

Characterization. N_2 and CO_2 physisorption were performed at 77 and 273 K, respectively, using a 3Flex pore analyzer (Micrometric Instruments Company). Prior to physisorption, PCFs were degassed at 90 °C for 1 h and 300 °C for 10 h to remove any surface adsorbents. Pore width distributions were calculated using non-local density functional theory (NLDFT). Micropore (<2 nm) and mesopore (2−50 nm) volumes in the fibers were measured using CO_2 and N_2 physisorption, respectively (Table S1). Light absorption spectra were acquired using a UV−vis−NIR spectrophotometer (Agilent Cary 5000). The ion concentrations were tracked with an inductively coupled plasma mass spectrometer (Agilent 7900 ICP-MS). Field-emission scanning electron microscopy (FE-SEM, LEO 1550) was utilized to image the carbon fibers. An acceleration voltage of 2 kV and a working distance of ∼3 mm were used. The SEM images were then processed using the ImageJ software. Differential scanning calorimetry (DSC, Discovery DSC2500, TA Instruments) was performed to determine the enthalpy of water evaporation and boiling points in various PCFs. Dry PCF mats were first studied using DSC, which showed zero heat flows. The PCF fiber mats were then submerged in water for ∼24 h to ensure water saturation. Afterward, the PCF fiber mats were loaded immediately into DSC pans and weighed with an analytical balance. Immediately following the weighing, the PCF mats were heated from room temperature to 120 °C at a rate of 10 °C min^{-1}. After the DSC scan, the residual weight of PCF was measured. The difference was used to calculate the weight of water evaporated. By utilizing the weight of evaporated water and the integral of heat flow, the amount of energy required to evaporate a unit mass of water adsorbed on the PCF was calculated (Figure 5b). DSC was calibrated using indium [melting point (m.p.) = 156.60 °C] and zinc (m.p. = 419.47 °C) standards. The boiling point was measured as the midpoint of the endothermic peak.

Evaporation Performance Testing. Water evaporation experiments were conducted using a solar simulator (Newport 3 M) with an output power of 1000 W m^{-2} (1 sun irradiation) in a dark room. A power meter (Newport ORIEL Sol3A) controlled the output of the solar simulator. Each solar desalination sample was tested in Petri dishes along with a blank water sample as a control. The carbon fiber bundles were placed in a small cork support to ensure that they floated at the water-air interface. The mass loss of water was monitored using an analytical balance with a 0.01 mg resolution. Water vapor was condensed along a glass dome. Salt concentrations were measured with ICP-MS to track common ions within saltwater (Na^+, Mg^{2+}, K^+, and Ca^{2+}) before and after desalination. Energy efficiency (η) for solar to vapor generation was calculated according to the following equation:

$$\eta = (mH_{vap})/(C_{opt}P_0) \quad (1)$$

where m is the mass flux, H_{vap} is the vaporization enthalpy of water, C_{opt} is the optical concentration on the absorber surface, and P_0 is the solar irradiation of 1 sun (1000 W m^{-2}). The desalination rates were normalized to geometric surface area of each fiber mat exposed to the solar irradiation. Exposed area was calculated by measuring the sides and top of the carbon fiber mats above the floating material (cork).

RESULTS AND DISCUSSION

Using reversible addition-fragmentation chain transfer (RAFT) polymerization, we synthesized PAN homopolymers and PMMA-*b*-PAN block copolymers based on our previous report.[48] The molecular weight and composition of PMMA-*b*-PAN control the surface area and mesopore size distribution of PCFs. In general, high molecular weights and volume fractions (φ_{PMMA}) of PMMA result in large mesopore sizes. Specifically, both larger φ_{PMMA} and longer PMMA chains provide larger pores in the PCF, whereas larger PAN chains and φ_{PAN} develop more graphitic and disordered carbon matrices. The overall molecular weight also affects the surface area and spinnability of the fibers.[48] Due to the unique cross-linking characteristics of PAN, the block copolymer could not reach an equilibrium state to form any of the classical block copolymer morphologies.[48] Thus, three PMMA-*b*-PAN polymers were synthesized with number average molecular weights (M_n) of 108-*b*-44, 59-*b*-36, and 41-*b*-66 kDa (Figure S1) to produce three types of PCFs, designated as PCF-A, PCF-B, and PCF-C, respectively (Table 2). As a control, PAN with M_n = 46 kDa was also synthesized to produce microporous CFs. As reported previously,[50] PAN with M_n in the range of 13−215 kDa produced CFs with similar properties.

Table 2. Characteristics of Polymer Precursors from RAFT Polymerization

polymer	M_n, PMMA (kDa)	M_n, PAN (kDa)	φ_{PAN}[a]	PDI[b]	corresponding fibers
PAN		46	1	1.19	CF
BCP-A	108	44	0.29	1.17	PCF-A
BCP-B	59	36	0.37	1.15	PCF-B
BCP-C	41	66	0.59	1.10	PCF-C

[a]Volume fraction of PAN. [b]Polydispersity index.

The polymers were electrospun into fibers, which were then sequentially oxidized in air and pyrolyzed under N_2 to produce PCFs and CFs (Figure 1c). The fiber bundles exhibited nonuniform inter-fiber distances (Figure 2a−d). Since the capillary height is inversely proportional to the radius of a capillary, the inter-fiber gaps can act as channel-like macropores to efficiently transport water for desalination, analogous to the hydrophilic macroporous channels that benefited water transport *via* arterial pumping in a previous report.[49]

In addition to the macropores, PCFs displayed distinct ubiquitous mesopores, both on the skin surfaces (Figure 2a−c) and in the cross sections (Figure 2e−g). The PAN block served as the primary carbon source during pyrolysis, whereas the PMMA block acted as a sacrificial component to produce well-dispersed, uniform mesopores *via* thermodynamically driven microphase separation and thermal decomposition.[48] Contrastingly, the PAN-derived CFs were devoid of any visible mesopores (Figure 2d,h).

https://doi.org/10.1021/acs.macromol.2c00092
Macromolecules 2022, 55, 4803−4811

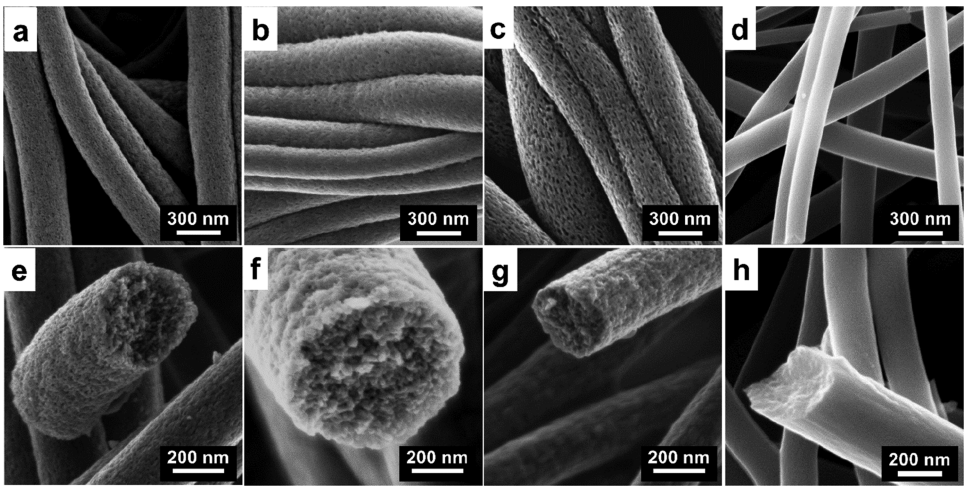

Figure 2. Representative SEM images of the outer surface (a–d) and cross section (e–h) of (a, e) PCF-A, (b, f) PCF-B, (c, g) PCF-C, and (d, h) CF.

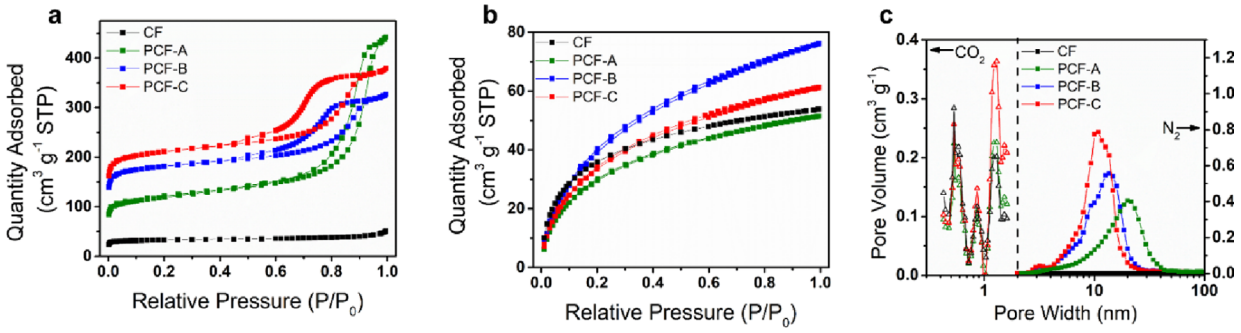

Figure 3. (a) N_2 and (b) CO_2 physisorption isotherms and (c) pore width distributions of PCF-A, PCF-B, PCF-C, and CF. The pore distributions were plots with a double-Y plot for pore volume based on CO_2 derived physisorption (left, plotted with triangles) and N_2 derived physisorption (right, square).

Gas physisorption analysis revealed the pore widths and surface areas of the PCFs and CFs (Figure 3). The N_2 and CO_2 isotherms of all PCFs exhibited type IV and I characteristics, respectively, as defined by the International Union of Pure and Applied Chemistry (IUPAC).[51] Micropore (<2 nm) and mesopore (2–50 nm) volumes in the fibers were measured using CO_2 and N_2 physisorption, respectively (Table S1). Specifically, the N_2 sorption of PCFs showed hysteresis at $0.6 < P/P_0 < 0.9$, indicating the presence of mesopores (Figure 3a). On the other hand, the isotherms of CFs had type II and type I characteristics for N_2 and CO_2 adsorption, respectively, suggesting the absence of mesopores but the presence of micropores. Nevertheless, the similar type I isotherms of CO_2 sorption signified that both PCFs and CFs contained micropores of similar pore widths (Figure 3b).

Using non-local density functional theory (NLDFT),[52] the pore width distributions were calculated (Figure 3c).[48] During carbonization, the carbon matrices of all PCFs and CFs developed micropores in trimodal peaks centered at ~0.58, 0.86, and 1.2 nm (Figure 3c).[53] PCF-A, PCF-B, and PCF-C also showed unimodal mesopore peaks at 21.6, 14.7, and 10.7 nm, respectively. The pore widths in the range of ~0.5–22 nm allowed for investigating the effects of pore width effects on water vaporization (Table S1).

Using PCFs and CFs with different pore size distributions, the effects of nanoconfinement on solar desalination performance were studied. After pyrolysis, all PCFs and CFs absorbed >99% of the solar spectrum wavelengths (Figure 4a). The fibers were placed at the water-air interface of saltwater (35 g L^{-1} NaCl), supported with a floating cork. Under 1 sun irradiation, weight loss due to water evaporation was tracked over time. The measured change in water mass over about 6 h revealed an increasing evaporation rate in the order of blank water, CF, PCF-A, PCF-B, and PCF-C (Figure 4b). The PCF and CF required ~680 s of heating under solar irradiation to reach a steady state and achieve a linear evaporation rate owing to the characteristic thermal diffusivity (Figure S2) and initial heating.[22] The evaporation rates were normalized to the fiber mat surface area exposed to sunlight (*i.e.*, geometrical area) and are reported in units of water evaporated per unit area per unit time (Figure 4c). PCF-C displayed the highest desalination rate of 3.8 kg m^{-2} h^{-1}.

The energy efficiency (η) for solar vapor generation was calculated according to the following equation (eq 1). To calculate the energy efficiency, H_{vap} was estimated by both differential scanning calorimetry (DSC) and dark-field evaporation (Figure S3). The highest performing fibers (PCF-C) reached an energy efficiency of ~94% (based on the enthalpy measured by DSC, *vide infra*).

The desalination rate was positively correlated with the pore volume and surface area calculated using the Brunauer–Emmett–Teller (BET) theory (Figure 4d). The micropore volumes were similar among the carbon fibers. In contrast, the mesopore volumes showed a stronger correlation with the

https://doi.org/10.1021/acs.macromol.2c00092
Macromolecules 2022, 55, 4803–4811

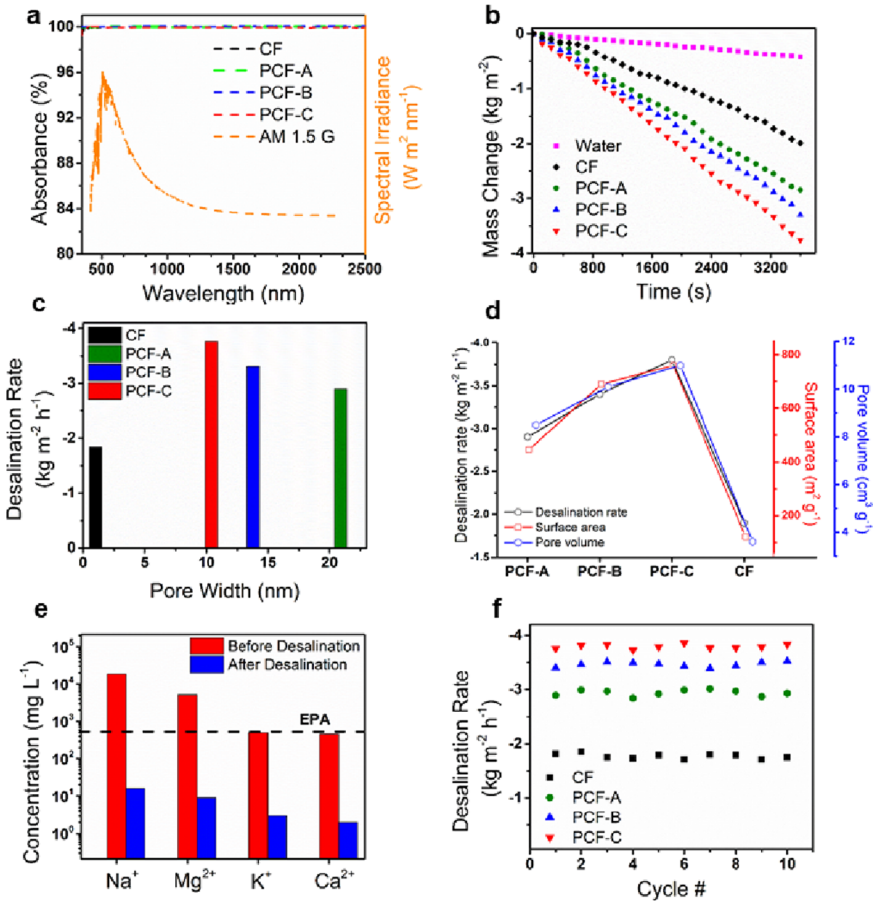

Figure 4. (a) UV−vis absorption spectra of PCFs and CFs overlaid with an AM 1.5 G solar irradiation spectrum. (b) Mass loss over time under 1 sun irradiation using PCFs and CFs as solar desalination materials, compared to a water-only cell (labeled as "water"). (c) Desalination rate against the average pore width of PCFs and CFs. (d) Desalination rate against the surface area and pore volume of PCFs and CFs. (e) ICP-MS analysis of four common ions in saltwater before and after desalination using PCF-C. The black dashed line highlights the U.S. Environmental Protection Agency (EPA) safe drinking water level. (f) Reusability of PCFs and CFs over 10 cycles (2 h per cycle).

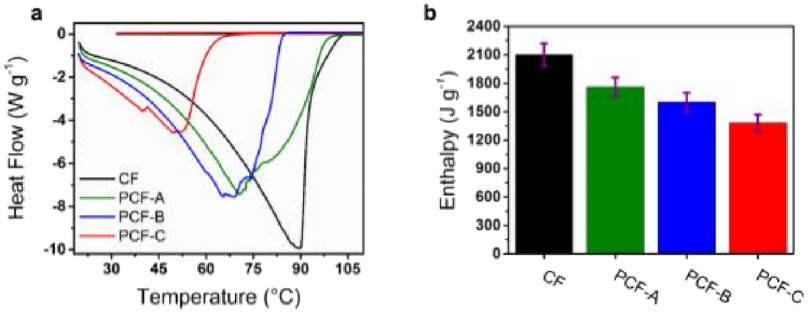

Figure 5. (a) Differential scanning calorimetry (DSC) traces for water confined in CFs and PCFs. (b) Equivalent water vaporization enthalpy calculated from the DCS curves. Error bars are standard deviations.

increasing desalination rates (Figure S4). To reveal the purity of evaporated water, inductively coupled plasma mass spectrometry (ICP-MS) was used to probe the salinity of four common ions, including Na^+, Mg^{2+}, K^+, and Ca^{2+}, before and after desalination. The pre-evaporated saltwater solution contained 1.9×10^4 mg L^{-1} Na^+, 6.5×10^3 mg L^{-1} Mg^{2+}, 5.7×10^2 mg L^{-1} K^+, and 5.1×10^2 mg L^{-1} Ca^{2+}. However, the distillate after evaporation showed order-of-magnitude reduction in ion concentrations (Figure 4e). The concentrations of Na^+, Mg^{2+}, K^+, and Ca^{2+} were all below 11 mg L^{-1}, meeting the standard of drinking water set by the U.S. Environmental Protection Agency (Figure 4e).[54]

Practical solar desalination requires the solar absorbers to be robust and sustainable under continuous irradiation in high saline water. The PCF and CF performance remained stable under irradiation, evident by their constant evaporation rates (Figure 4f). The vaporization rates were tested over 10 cycles for each type of PCF and CF. During each cycle, fresh saltwater was refilled into the desalination testing cell and irradiated continuously. The PCFs also showed facile self-cleaning ability and negligible efficiency loss. When not in use, salts might precipitate along the exterior of the fibers. The ability for salt resistance or self-cleaning material directly impacts the continuous use of solar desalination systems.[55]

https://doi.org/10.1021/acs.macromol.2c00092
Macromolecules 2022, 55, 4803−4811

However, once the fibers were placed in saline water, the salts quickly dissolved because the fibers were hydrophilic and the pores facilitated water transport to wet the fibers (Figure S5).

The well-defined hierarchical pores in the PCFs permitted investigations into the influence of surface area, pore volume, and pore size on desalination, a fundamental understanding of which is crucial for designing future solar thermal materials. Water confined in the pores of PCFs and CFs was analyzed with differential scanning calorimetry (DSC) using a temperature scan from room temperature to 120 °C under a heating rate of 10 °C s^{-1} (Figure 5a). By integrating the heat flow vs time, the enthalpy of water vaporization within the CFs and PCFs was estimated. The CFs showed an endothermic peak with an intensity of approximately −10 W g^{-1} at 89 °C. The peak endothermic temperature further decreased in the order of PCF-A, PCF-B, and PCF-C, to 74, 71, and 52 °C, respectively (Figure 5a). For PCF-A, PCF-B, and PCF-C, the peak heat flows decreased progressively to −7.7, −7.8, and −4.6 W g^{-1} (Figure 5a), corresponding to vaporization enthalpies (H_{vap}) of ∼1760, 1600, and 1380 J g^{-1} (Figure 5b), respectively. The vaporization enthalpies were calculated based on the weight of water evaporated (Table S2, m1 - m2).

In addition, the mass of the water within the carbon fibers was monitored with DSC (Table S2). The soaked PCF fibers adsorbed ∼10× their weight in water, which aligns with the combined pore volume estimates by CO_2 and N_2 physisorption. Based on the weight of the water and the integrated DSC trace, the enthalpy was directly estimated by the input of energy (J) into the system. Consistently, the PCF fibers showed a lower energy input for evaporation of water within the DSC pans (Table S2).

Hydrogen bonding is a major contributor to the cohesion among water molecules and the H_{vap} of water. Previous research into water confinement shows hydrogen bond disruption in pores with widths <100 nm.[36] In carbonized materials, pores of <100 nm also contribute to reduced enthalpy.[43,45−47] In this work, the CFs and PCFs conferred different confinement effects on water molecules due to the different porous structures. For bulk water, the vaporization enthalpy at 25 °C and standard pressure is ∼2440 J g^{-1}. With inter-fiber distances and micropores, the H_{vap} of water in the CF was reduced to ∼2100 J g^{-1} based on DSC, which provided an estimation of enthalpy without mesopores (Figure S6 and Table S3). Upon the addition of mesopores, the surface area and pore volume of the carbon fibers increased. The culmination of inter-fiber distances, mesopores, and micropores resulted in a larger reduction in H_{vap}. The reduced enthalpy delves into two confinement factors: the disruption of the hydrogen bonding network of water molecules and the development of smaller capillary structures within the mesopores.[56] In addition, the mesopores also contribute a tertiary beneficial factor in a lower thermal diffusivity within the PCFs (Figure S2). Notably, PCF-C had the smallest H_{vap}. The reduction in H_{vap} determined by DSC was also confirmed by dark-environment (dark-field) evaporation, with the CFs and PCFs following an identical trend (Figure S3). Owing to the mesopore-related reduction in H_{vap}, all PCFs displayed high solar desalination rates. The smaller the mesopores, the more reduction in H_{vap} observed and thus the higher the solar desalination rates. However, this effect diminished in the CFs that had only micropores. Notably, both CFs and PCFs possessed macropores (inter-fiber voids due to fiber processing), which aided water transport.

The PCFs with mesopores speed up water evaporation (Figure 5a) by suppressing hydrogen bonds to the extent that the vaporization enthalpy of water is significantly reduced, but at the same time, water can still evaporate as clusters.[57] On the other hand, the micropores in the CFs had widths from 0.58 to 1.2 nm, which could only accommodate two to four water molecules in their cross sections. As a result, the hydrogen bond network is effectively destroyed, and the cluster evaporation mechanism diminishes. In addition, water transport is hindered due to the small size of micropores as well as the hydrophilic nature of the pore walls. Thus, the value of H_{vap} of the CFs is greater than that of the mesopore-containing PCFs. Because of the decreased water transport, the lower surface area, and the suppression of the cluster evaporation mechanism, the CFs exhibited limited desalination performance.

Nanoconfinement causes a disruption in the continuous hydrogen-bonding network, which plays an important role in the physical properties of water. For example, previous studies showed that nanoconfinement could produce water in a variety of bonding states (*e.g.*, network water, intermediate water, and multimer water) with differing vaporization enthalpy.[49] As expected, it requires less energy to vaporize small water clusters collectively than to break each hydrogen bond and vaporize each water molecule individually.[58]

In addition to the nanoconfinement effects, the hierarchical porous structure of the PCFs provides an important factor for continuous desalination. Vaporization of water in porous media follows two stages. In the first stage, water flows from the bulk into the pores through capillary actions, and in the second stage, water evaporates and the air-water interface recedes on the pore surface.[59] The air-water interface is vital for water evaporation.[60] The vapor phase above the receding air-water interface quickly saturates, resulting in a concentration gradient of water vapor toward the bulk air. The concentration gradient becomes the driving force for water vapor molecules to escape the porous network and enter air.[61] In both stages, the pore tortuosity, geometry, and size distribution affect water transport as well as evaporation rates and efficiency.[62] The transport of water vapor from micropores to mesopores and then to macropores provides a "capillary valve effect", further facilitating vapor release and water evaporation. The slightly hydrophilic nature of the PCFs, combined with the capillary pressure in the hierarchical pores, allows a continuous film to develop, thus increasing the air-water interfacial area and leading to high desalination rates.[63]

■ CONCLUSIONS

In summary, block copolymer-based porous carbon fibers were demonstrated to be highly efficient materials for solar desalination. Importantly, the well-defined interconnected pores allowed for delineation of the nanoconfinement effects of mesopores and micropores on water vaporization enthalpy. The carbon fibers showed strong light absorption of >99% across the entire solar spectrum, thereby providing high light-to-thermal energy conversion efficiency. The nanoconfinement reduced the enthalpy of water vaporization, and the effect varied with the pore size, surface area, and pore volume. In general, the enthalpy decreased as the mesopore size decreased. However, the enthalpy started to increase as the pore size was further reduced to the micropore range. The porous carbon fibers with a mesopore size of 10.7 nm were found to have the lowest water vaporization enthalpy and the

https://doi.org/10.1021/acs.macromol.2c00092
Macromolecules 2022, 55, 4803−4811

highest desalination rate of 3.8 kg m^{-2} h^{-1} under 1 sun irradiation, which was hitherto unprecedented in the literature, for single-stage solar desalination devices.

In addition to high solar desalination rates, the porous carbon fibers exhibited excellent reusability and stability. Thus, this study highlighted the potency porous carbon fibers, as an exciting emerging material, to achieve high solar efficiency, high vaporization rate, and high sustainability. These materials have great potential for desalination, separation, filtration, and other environmental applications.

■ ASSOCIATED CONTENT

Supporting Information

The Supporting Information is available free of charge at https://pubs.acs.org/doi/10.1021/acs.macromol.2c00092.

Size exclusion chromatography of polymer precursors, dark-field evaporation, scheme of water vaporization enthalpy reduction, self-cleaning of block copolymer-based porous carbon fibers, and thermal diffusivity of carbon fibers (PDF)

■ AUTHOR INFORMATION

Corresponding Author

Guoliang Liu − *Department of Chemistry, Macromolecules Innovations Institute, and Division of Nanoscience, Academy of Integrated Science, Virginia Tech, Blacksburg, Virginia 24061, United States;* orcid.org/0000-0002-6778-0625; Email: gliu1@vt.edu

Authors

Joel M. Serrano − *Department of Chemistry, Virginia Tech, Blacksburg, Virginia 24061, United States;* orcid.org/0000-0002-1508-5508

Tianyu Liu − *Department of Chemistry, Virginia Tech, Blacksburg, Virginia 24061, United States;* orcid.org/0000-0002-8716-749X

Dong Guo − *Department of Chemistry, Virginia Tech, Blacksburg, Virginia 24061, United States;* orcid.org/0000-0002-3469-2602

Zacary L. Croft − *Department of Chemistry, Virginia Tech, Blacksburg, Virginia 24061, United States*

Ke Cao − *Macromolecules Innovations Institute, Virginia Tech, Blacksburg, Virginia 24061, United States;* orcid.org/0000-0001-7204-7455

Assad U. Khan − *Department of Chemistry, Virginia Tech, Blacksburg, Virginia 24061, United States;* orcid.org/0000-0001-6455-3219

Zhen Xu − *Department of Chemistry, Virginia Tech, Blacksburg, Virginia 24061, United States*

Elsaid Nouh − *Department of Chemistry, Virginia Tech, Blacksburg, Virginia 24061, United States*

Shengfeng Cheng − *Macromolecules Innovations Institute, Department of Physics, Center for Soft Matter and Biological Physics, and Department of Mechanical Engineering, Virginia Tech, Blacksburg, Virginia 24061, United States;* orcid.org/0000-0002-6066-2968

Complete contact information is available at: https://pubs.acs.org/10.1021/acs.macromol.2c00092

Notes

The authors declare no competing financial interest.

■ ACKNOWLEDGMENTS

We acknowledge the use of the Nanoscale Characterization and Fabrication Laboratory (NCFL) and chemistry facilities at Virginia Tech. We also acknowledge Yuqing Li for assistance with thermal diffusion testing of the carbon fibers as well as the toxicology lab and McAlister Council-Troche for aid in preparing ICP samples. This material is based on the work supported by the National Science Foundation under the award number DMR1752611 through the CAREER award and the American Chemical Society Petroleum Research Foundation through the DNI award.

■ REFERENCES

(1) Elimelech, M.; Phillip, W. A. The future of seawater desalination: energy, technology, and the environment. *Science* **2011**, *333*, 712−717.

(2) Shannon, M. A.; Bohn, P. W.; Elimelech, M.; Georgiadis, J. G.; Mariñas, B. J.; Mayes, A. M. Science and technology for water purification in the coming decades. *Nature* **2008**, *452*, 301−310.

(3) Liu, N.; Hao, L.; Zhang, B.; Niu, R.; Gong, J.; Tang, T. Rational Design of High-Performance Bilayer Solar Evaporator by Using Waste Polyester-Derived Porous Carbon-Coated Wood. *Energy Environ. Mater.* **2021**, DOI: 10.1002/eem2.12199.

(4) Wang, Z.; Horseman, T.; Straub, A. P.; Yip, N. Y.; Li, D.; Elimelech, M.; Lin, S. Pathways and challenges for efficient solar-thermal desalination. *Sci. Adv.* **2019**, *5*, No. eaax0763.

(5) Yao, Y.; Zhang, P.; Jiang, C.; DuChanois, R. M.; Zhang, X.; Elimelech, M. High performance polyester reverse osmosis desalination membrane with chlorine resistance. *Nat. Sustainability* **2021**, *4*, 138−146.

(6) Di Vincenzo, M.; Tiraferri, A.; Musteata, V. E.; Chisca, S.; Sougrat, R.; Huang, L. B.; Nunes, S. P.; Barboiu, M. Biomimetic artificial water channel membranes for enhanced desalination. *Nat. Nanotechnol.* **2021**, *16*, 190−196.

(7) Jang, D.; Idrobo, J. C.; Laoui, T.; Karnik, R. Water and Solute Transport Governed by Tunable Pore Size Distributions in Nanoporous Graphene Membranes. *ACS Nano* **2017**, *11*, 10042−10052.

(8) Wu, Y.; Fu, C. F.; Huang, Q.; Zhang, P.; Cui, P.; Ran, J.; Yang, J.; Xu, T. 2D Heterostructured Nanofluidic Channels for Enhanced Desalination Performance of Graphene Oxide Membranes. *ACS Nano* **2021**, *15*, 7586−7595.

(9) Buonomenna, M. G. Nano-enhanced reverse osmosis membranes. *Desalination* **2013**, *314*, 73−88.

(10) Kerdi, S.; Qamar, A.; Alpatova, A.; Ghaffour, N. An in-situ technique for the direct structural characterization of biofouling in membrane filtration. *J. Membr. Sci.* **2019**, *583*, 81−92.

(11) Kim, S.; Piao, G.; Han, D. S.; Shon, H. K.; Park, H. Solar desalination coupled with water remediation and molecular hydrogen production: a novel solar water-energy nexus. *Energy Environ. Sci.* **2018**, *11*, 344−353.

(12) Tao, P.; Ni, G.; Song, C.; Shang, W.; Wu, J.; Zhu, J.; Chen, G.; Deng, T. Solar-driven interfacial evaporation. *Nat. Energy* **2018**, *3*, 1031−1041.

(13) Xu, W.; Xing, Y.; Liu, J.; Wu, H.; Cui, Y.; Li, D.; Guo, D.; Li, C.; Liu, A.; Bai, H. Efficient Water Transport and Solar Steam Generation via Radially, Hierarchically Structured Aerogels. *ACS Nano* **2019**, *13*, 7930−7938.

(14) Kuang, Y.; Chen, C.; He, S.; Hitz, E. M.; Wang, Y.; Gan, W.; Mi, R.; Hu, L. A High-Performance Self-Regenerating Solar Evaporator for Continuous Water Desalination. *Adv. Mater.* **2019**, *31*, No. e1900498.

(15) Lu, Y.; Fan, D.; Wang, Y.; Xu, H.; Lu, C.; Yang, X. Surface Patterning of Two-Dimensional Nanostructure-Embedded Photothermal Hydrogels for High-Yield Solar Steam Generation. *ACS Nano* **2021**, *15*, 10366−10376.

(16) Chandrashekara, M.; Yadav, A. Water desalination system using solar heat: A review. *Renewable Sustainable Energy Rev.* **2017**, *67*, 1308−1330.
(17) Nagar, A.; Pradeep, T. Clean Water through Nanotechnology: Needs, Gaps, and Fulfillment. *ACS Nano* **2020**, *14*, 6420−6435.
(18) Liu, Z.; Zhou, Z.; Wu, N.; Zhang, R.; Zhu, B.; Jin, H.; Zhang, Y.; Zhu, M.; Chen, Z. Hierarchical Photothermal Fabrics with Low Evaporation Enthalpy as Heliotropic Evaporators for Efficient, Continuous, Salt-Free Desalination. *ACS Nano* **2021**, 13007.
(19) Li, R.; Zhang, L.; Shi, L.; Wang, P. MXene Ti3C2: An Effective 2D Light-to-Heat Conversion Material. *ACS Nano* **2017**, *11*, 3752−3759.
(20) Li, Y.; Gao, T.; Yang, Z.; Chen, C.; Kuang, Y.; Song, J.; Jia, C.; Hitz, E. M.; Yang, B.; Hu, L. Graphene oxide-based evaporator with one-dimensional water transport enabling high-efficiency solar desalination. *Nano Energy* **2017**, *41*, 201−209.
(21) Zhang, Q.; Yi, G.; Fu, Z.; Yu, H.; Chen, S.; Quan, X. Vertically Aligned Janus MXene-Based Aerogels for Solar Desalination with High Efficiency and Salt Resistance. *ACS Nano* **2019**, *13*, 13196−13207.
(22) Kim, K.; Yu, S.; An, C.; Kim, S. W.; Jang, J. H. Mesoporous Three-Dimensional Graphene Networks for Highly Efficient Solar Desalination under 1 sun Illumination. *ACS Appl. Mater. Interfaces* **2018**, *10*, 15602−15608.
(23) Zielinski, M. S.; Choi, J.-W.; La Grange, T.; Modestino, M.; Hashemi, S. M. H.; Pu, Y.; Birkhold, S.; Hubbell, J. A.; Psaltis, D. Hollow mesoporous plasmonic nanoshells for enhanced solar vapor generation. *Nano Lett.* **2016**, *16*, 2159−2167.
(24) Zhou, L.; Tan, Y.; Ji, D.; Zhu, B.; Zhang, P.; Xu, J.; Gan, Q.; Yu, Z.; Zhu, J. Self-assembly of highly efficient, broadband plasmonic absorbers for solar steam generation. *Sci. Adv.* **2016**, *2*, No. e1501227.
(25) Xu, J.; Xu, F.; Qian, M.; Li, Z.; Sun, P.; Hong, Z.; Huang, F. Copper nanodot-embedded graphene urchins of nearly full-spectrum solar absorption and extraordinary solar desalination. *Nano Energy* **2018**, *53*, 425−431.
(26) Bae, K.; Kang, G.; Cho, S. K.; Park, W.; Kim, K.; Padilla, W. J. Flexible thin-film black gold membranes with ultrabroadband plasmonic nanofocusing for efficient solar vapour generation. *Nat. Commun.* **2015**, *6*, 10103.
(27) Chang, C.; Tao, P.; Fu, B.; Xu, J.; Song, C.; Wu, J.; Shang, W.; Deng, T. Three-Dimensional Porous Solar-Driven Interfacial Evaporator for High-Efficiency Steam Generation under Low Solar Flux. *ACS Omega* **2019**, *4*, 3546−3555.
(28) Morciano, M.; Fasano, M.; Bergamasco, L.; Albiero, A.; Lo Curzio, M.; Asinari, P.; Chiavazzo, E. Sustainable freshwater production using passive membrane distillation and waste heat recovery from portable generator sets. *Appl. Energy* **2020**, *258*, No. 114086.
(29) Liu, X.; Liu, H.; Yu, X.; Zhou, L.; Zhu, J. Solar thermal utilizations revived by advanced solar evaporation. *Curr. Opin. Chem. Eng.* **2019**, *25*, 26−34.
(30) Wu, L.; Dong, Z.; Cai, Z.; Ganapathy, T.; Fang, N. X.; Li, C.; Yu, C.; Zhang, Y.; Song, Y. Highly efficient three-dimensional solar evaporator for high salinity desalination by localized crystallization. *Nat. Commun.* **2020**, *11*, 521.
(31) Xu, W.; Hu, X.; Zhuang, S.; Wang, Y.; Li, X.; Zhou, L.; Zhu, S.; Zhu, J. Flexible and Salt Resistant Janus Absorbers by Electrospinning for Stable and Efficient Solar Desalination. *Adv. Energy Mater.* **2018**, *8*, 1702884.
(32) Li, C.; Jiang, D.; Huo, B.; Ding, M.; Huang, C.; Jia, D.; Li, H.; Liu, C.-Y.; Liu, J. Scalable and robust bilayer polymer foams for highly efficient and stable solar desalination. *Nano Energy* **2019**, *60*, 841−849.
(33) Guan, W.; Guo, Y.; Yu, G. Carbon Materials for Solar Water Evaporation and Desalination. *Small* **2021**, *17*, No. e2007176.
(34) Tao, J.; Song, X.; Zhao, T.; Zhao, S.; Liu, H. Confinement effect on water transport in CNT membranes. *Chem. Eng. Sci.* **2018**, *192*, 1252−1259.
(35) Ruiz-Barragan, S.; Muñoz-Santiburcio, D.; Marx, D. Nano-confined Water within Graphene Slit Pores Adopts Distinct Confinement-Dependent Regimes. *J. Phys. Chem. Lett.* **2019**, *10*, 329−334.
(36) Knight, A. W.; Kalugin, N. G.; Coker, E.; Ilgen, A. G. Water properties under nano-scale confinement. *Sci. Rep.* **2019**, *9*, 8246.
(37) Shaat, M.; Javed, U.; Faroughi, S. Wettability and confinement size effects on stability of water conveying nanotubes. *Sci. Rep.* **2020**, *10*, 17167.
(38) Zhu, M.; Li, Y.; Chen, G.; Jiang, F.; Yang, Z.; Luo, X.; Wang, Y.; Lacey, S. D.; Dai, J.; Wang, C.; Jia, C.; Wan, J.; Yao, Y.; Gong, A.; Yang, B.; Yu, Z.; Das, S.; Hu, L. Tree-Inspired Design for High-Efficiency Water Extraction. *Adv. Mater.* **2017**, *29*, 1704107.
(39) Bian, Y.; Du, Q.; Tang, K.; Shen, Y.; Hao, L.; Zhou, D.; Wang, X.; Xu, Z.; Zhang, H.; Zhao, L.; Zhu, S.; Ye, J.; Lu, H.; Yang, Y.; Zhang, R.; Zheng, Y.; Gu, S. Solar Vapor-Generation: Carbonized Bamboos as Excellent 3D Solar Vapor-Generation Devices (Adv. Mater. Technol. 4/2019). *Adv. Mater. Technol.* **2019**, *4*, 1970020.
(40) Bian, Y.; Shen, Y.; Tang, K.; Du, Q.; Hao, L.; Liu, D.; Hao, J.; Zhou, D.; Wang, X.; Zhang, H.; Li, P.; Sang, Y.; Yuan, X.; Zhao, L.; Ye, J.; Liu, B.; Lu, H.; Yang, Y.; Zhang, R.; Zheng, Y.; Xiong, X.; Gu, S. Carbonized Tree-Like Furry Magnolia Fruit-Based Evaporator Replicating the Feat of Plant Transpiration. *Global Challenges* **2019**, *3*, 1900040.
(41) Liu, K. K.; Jiang, Q.; Tadepalli, S.; Raliya, R.; Biswas, P.; Naik, R. R.; Singamaneni, S. Wood-Graphene Oxide Composite for Highly Efficient Solar Steam Generation and Desalination. *ACS Appl. Mater. Interfaces* **2017**, *9*, 7675−7681.
(42) Zhou, X.; Zhao, F.; Guo, Y.; Zhang, Y.; Yu, G. A hydrogel-based antifouling solar evaporator for highly efficient water desalination. *Energy Environ. Sci.* **2018**, *11*, 1985−1992.
(43) Guan, Q. F.; Han, Z. M.; Ling, Z. C.; Yang, H. B.; Yu, S. H. Sustainable Wood-Based Hierarchical Solar Steam Generator: A Biomimetic Design with Reduced Vaporization Enthalpy of Water. *Nano Lett.* **2020**, *20*, 5699−5704.
(44) Coudert, F.-X.; Boutin, A.; Fuchs, A. H. Open questions on water confined in nanoporous materials. *Commun. Chem.* **2021**, *4*, 1.
(45) Ding, T.; Zhou, Y.; Ong, W. L.; Ho, G. W. Hybrid solar-driven interfacial evaporation systems: Beyond water production towards high solar energy utilization. *Mater. Today* **2021**, *42*, 178−191.
(46) Yang, M. Q.; Tan, C. F.; Lu, W.; Zeng, K.; Ho, G. W. Spectrum Tailored Defective 2D Semiconductor Nanosheets Aerogel for Full-Spectrum-Driven Photothermal Water Evaporation and Photochemical Degradation. *Adv. Funct. Mater.* **2020**, *30*, 2004460.
(47) Meng, F. L.; Gao, M.; Ding, T.; Yilmaz, G.; Ong, W. L.; Ho, G. W. Modular Deformable Steam Electricity Cogeneration System with Photothermal, Water, and Electrochemical Tunable Multilayers. *Adv. Funct. Mater.* **2020**, *30*, 2002867.
(48) Zhou, Z.; Liu, T.; Khan, A. U.; Liu, G. Block copolymer-based porous carbon fibers. *Sci. Adv.* **2019**, *5*, No. eaau6852.
(49) Serrano, J. M.; Khan, A. U.; Liu, T.; Xu, Z.; Esker, A. R.; Liu, G. Capacitive Organic Dye Removal by Block Copolymer Based Porous Carbon Fibers. *Adv. Mater. Interfaces* **2020**, *7*, 2000507.
(50) Serrano, J. M.; Liu, T.; Khan, A. U.; Botset, B.; Stovall, B. J.; Xu, Z.; Guo, D.; Cao, K.; Hao, X.; Cheng, S.; Liu, G. Composition Design of Block Copolymers for Porous Carbon Fibers. *Chem. Mater.* **2019**, *31*, 8898−8907.
(51) Thommes, M.; Kaneko, K.; Neimark, A. V.; Olivier, J. P.; Rodriguez-Reinoso, F.; Rouquerol, J.; Sing, K. S. W. Physisorption of gases, with special reference to the evaluation of surface area and pore size distribution (IUPAC Technical Report). *Pure Appl. Chem.* **2015**, *87*, 1051−1069.
(52) Bernet, T.; Piñeiro, M. M.; Plantier, F.; Miqueu, C. A 3D non-local density functional theory for any pore geometry. *Mol. Phys.* **2020**, *118*, No. e1767308.
(53) Zhou, Z.; Liu, T.; Khan, A. U.; Liu, G. Controlling the physical and electrochemical properties of block copolymer-based porous carbon fibers by pyrolysis temperature. *Mol. Syst. Des. Eng.* **2020**, *5*, 153−165.

https://doi.org/10.1021/acs.macromol.2c00092
Macromolecules 2022, 55, 4803−4811

(54) WHO *Guidelines for drinking-water quality*; 2011.
(55) Dong, X.; Cao, L.; Si, Y.; Ding, B.; Deng, H. Cellular Structured CNTs@SiO_2 Nanofibrous Aerogels with Vertically Aligned Vessels for Salt-Resistant Solar Desalination. *Adv. Mater.* **2020**, *32*, No. e1908269.
(56) Chen, C.; Duru, P.; Joseph, P.; Geoffroy, S.; Prat, M. Control of evaporation by geometry in capillary structures. From confined pillar arrays in a gap radial gradient to phyllotaxy-inspired geometry. *Sci. Rep.* **2017**, *7*, 1−8.
(57) Geistlinger, H.; Ding, Y.; Apelt, B.; Schlüter, S.; Küchler, M.; Reuter, D.; Vorhauer, N.; Vogel, H. J. Evaporation Study Based on Micromodel Experiments: Comparison of Theory and Experiment. *Water Resour. Res.* **2019**, *55*, 6653−6672.
(58) Le Caër, S.; Pin, S.; Esnouf, S.; Raffy, Q.; Renault, J. P.; Brubach, J.-B.; Creff, G.; Roy, P. A trapped water network in nanoporous material: the role of interfaces. *Phys. Chem. Chem. Phys.* **2011**, *13*, 17658−17666.
(59) A, M. M.; D, P. W.; E, K. A.; Sathyamurthy, R.; T, A. Different parameter and technique affecting the rate of evaporation on active solar still-a review. *Heat Mass Transfer* **2018**, *54*, 593−630.
(60) Shahraeeni, E.; Or, D. Pore-scale analysis of evaporation and condensation dynamics in porous media. *Langmuir* **2010**, *26*, 13924−13936.
(61) Lehmann, P.; Or, D. Evaporation and capillary coupling across vertical textural contrasts in porous media. *Phys. Rev. E: Stat., Nonlinear, Soft Matter Phys.* **2009**, *80*, No. 046318.
(62) Rose, D. A. Water movement in porous materials: Part 2-The separation of the components of water movement. *Br. J. Appl. Phys.* **1963**, *14*, 491.
(63) Keita, E.; Rodts, S.; Coussot, P. MRI evidence of nanoparticles migration in drying porous media. In *5th International Conference on Porous Media and Their Applications in Science, Engineering and Industry*; 2013.

https://doi.org/10.1021/acs.macromol.2c00092
Macromolecules 2022, 55, 4803−4811